

Structural and electrochemical studies of Au–Pt nanoalloys

Aurelien Habrioux,^a Walter Vogel,^b Maxime Guinel,^c Laure Guetaz,^c
Karine Servat,^a Boniface Kokoh^{*a} and Nicolas Alonso-Vante^{*a}

Received 19th November 2008, Accepted 6th February 2009

First published as an Advance Article on the web 3rd March 2009

DOI: 10.1039/b820668f

Carbon supported Au–Pt catalysts with different bimetallic compositions were prepared by water-in-oil (w/o) micro-emulsions. Carbon Vulcan XC-72R was added during the synthesis of particles in order to obtain good dispersion. Structural characterization was performed using XRD (X-ray diffraction) at wide angles, WAXS (wide-angle X-ray scattering) which showed that Pt–Au particles exhibited alloy properties in samples with high gold-content, and a segregation effect for those with low gold-content. Electrochemical characterization allowed estimation of the surface composition of Pt–Au alloys. These experiments have been confirmed by XRD data. Moreover, HRTEM (high resolution transmission electron microscopy) and XEDS (X-ray energy dispersive spectroscopy) characterization further confirmed the electrochemical results and XRD data. CO stripping experiments have shown an increasing bonding energy between CO and platinum with the gold content in the nanoalloys.

Introduction

Bimetallic structures have been widely investigated to develop new electrocatalysts with higher activity and low cost. A great deal of studies focus on platinum based nanoparticles. Among them Pt–Ru and Pt–Au nanoparticles exhibit high catalytic activity for electrochemical reactions, attributed to an electronic effect with a modification of the d-band center of platinum due to the formation of alloyed materials.^{1,2} In fact Pt–Au alloyed nanoparticles synthesized by microemulsions have demonstrated a great activity towards methanol oxidation or glucose oxidation. Since gold has been found to be catalytically active for CO oxidation³ it has been found interesting to study this reaction on Pt–Au catalysts. The activity of gold for CO oxidation could depend on the substrate used and on the size of the nanoparticles. Previous studies have shown that the shift of the CO oxidation peak depends on the surface composition, the particle size and the structure of the material. Accordingly, we aimed at satisfactorily characterizing several of the synthesized catalyst materials using transmission electron microscopy techniques. A complete characterization of the pertinent structure–catalytic property-relationships that give rise to the performance of these materials has proven to be difficult.^{4–6} Our objective was to understand better the structure and arrangement of these elements because their reactivity critically depends on it.^{2–4}

Experimental

Materials

Hydrogen tetrachloroaurate hydrate (HAuCl₄, 3H₂O, 99.9%, ACS reagent), trisodium citrate (99%, ACS reagent), Nafion, and tetraethyleneglycolmonododecylether (BRIJ[®] 30) were supplied by Sigma-Aldrich. Hexachloroplatinate (H₂PtCl₆, 6H₂O, 99.9%, ACS reagent) was purchased from Alfa-Aesar. The oil phase (*n*-heptane, 99%) and the reducing agent (NaBH₄, 99%) were provided by Acros-Organics. Supporting electrolytes were prepared with sodium dihydrogen phosphate monohydrate (NaH₂PO₄, H₂O), and di-sodium hydrogen phosphate (Na₂HPO₄) were supplied by Merck. D-Glucose (99%, pro-analysis) was also purchased from Merck. All the aqueous solutions were prepared using 18.2 MΩ cm Millipore-MilliQ water. Vulcan XC-72R was provided by Cabot.

Synthesis of gold-platinum nanoparticles

Gold-platinum bimetallic nanoparticles were synthesized in water-in-oil (w/o) microemulsion of ultrapure water–tetraethyleneglycol monododecylether–*n*-heptane.^{7,8} The reduction of Pt and Au ions was performed using sodium borohydride (NaBH₄) as reducing agent.⁹ The nanoparticles were formed by mixing two microemulsions with the same composition, one containing the precursor salts (H₂PtCl₆ or HAuCl₄ + H₂PtCl₆) and the other, the reducing agent. After the formation of Pt, Au or Au–Pt nanoparticles in the microemulsion, an appropriate amount of carbon Vulcan XC-72R was added under constant stirring for 2.5 h. The supported catalysts were separated, washed several times with acetone, ethanol and ultrapure water to eliminate excess of surfactant molecules and finally dried in vacuum over silica gel. The purpose of the addition of carbon Vulcan is to prevent the agglomeration of particles during elimination of the remaining surfactant.

^a Laboratory of Electrocatalysis, UMR-CNRS 6503, University of Poitiers, 40 Av. Recteur Pineau, F-86022 Poitiers, France.

E-mail: nicolas.alonso.vante@univ-poitiers.fr,
boniface.kokoh@univ-poitiers.fr;

Fax: +33 (0)54945 3580; Tel: +33 (0)54945 3625

^b Department of Chemistry, National Central University,
No. 300 Jung-Da Rd., Chung-Li, Taoyuan, 32001, Taiwan

^c CEA Grenoble, 17 Rue des Martyrs, 38054 Grenoble, France

Physical-chemical characterization of the catalysts

The synthesized catalyst materials (Pt, Au₃₀Pt₇₀, Au₇₀Pt₃₀, Au₈₀Pt₂₀ and Au) were characterized using transmission electron microscopy (TEM) techniques in order to determine size distributions, their morphologies, their crystallographic structures and their chemical compositions. Each material was sampled identically with a small amount of the active powder ultrasonically dispersed in anhydrous ethanol. The carbon-supported nanoparticles were collected by dipping Lacey-type carbon support films into the suspensions. The samples were examined using three complementary TEM equipments (JEOL 3010 and a JEOL 4000EX, and a probe corrected FEI-titan). The Titan is equipped with a lithium-drifted silicon detector for X-ray energy dispersive spectroscopy (XEDS). It is capable of producing a fine electron probe allowing for the direct identification and quantification of elements in individual nanoparticles.

X-Ray patterns were obtained with a Guinier powder diffractometer (HUBER), set at the 45° transmission position. A Johansson type Ge monochromator produces a focused monochromatic Cu K α_1 primary beam ($\lambda = 0.15406$ nm). The powder sample was slightly pressed and fixed between two 3 μ m polyethylene foils and measured immediately in ambient conditions. A scan of the pure Vulcan XC-72R support was used for the background correction. The background-corrected patterns were subjected to the usual angular correction for absorption, polarization and geometrical factors, and plotted *versus* the reciprocal scattering length $b = 2 \sin\theta/\lambda$ (θ , Bragg angle; λ , wavelength). Each diffraction peak was fitted with a Pearson VII function, eqn (1).¹⁰

$$f(b) = \frac{K_1}{[1 + K_2(b - K_3)^2]^{K_4}} \quad (1)$$

The four introduced coefficients (K_1 , K_2 , K_3 , K_4) were extracted by a Lewenberg–Marquardt algorithm. The integral line width of each peak was extracted from the fitted lines and reported *versus* the reciprocal scattering length. The value of K_4 is very close to 1, which means that the fitted line profile is near a Lorentzian one. Consequently, according to Warren's treatment of defective metals¹¹ the three different contributions to the integral line width broadening (size broadening, stacking fault broadening, and microstrain broadening) can be added linearly, eqn (2).^{10,12}

$$db = \frac{1}{d} + \frac{\alpha V_{hkl}}{a} + \frac{2\sigma b}{E_{hkl}} \quad (2)$$

with d mass mean crystalline size, V_{hkl} a constant depending on the miller indexes (h , k , l), a the lattice parameter, σ the micro stress, b the Bragg peak position in the reciprocal space and E_{hkl} the Young's modulus calculated from the elasticity coefficients for the materials.

Electrochemical measurements

All the electrochemical experiments were carried out using a computer controlled VoltaLab Potentiostat PGZ 402 Electrochemical Interface (Radiometer Analytical). For cyclic voltammetry, the working electrodes were composed of the metal/C catalysts deposited over glassy carbon (polished to a

mirror-finish prior to each experiment) disk of a rotating disk electrode. The experiments were performed in a conventional three-electrode Pyrex cell (17 mL). Hg–Hg₂SO₄–K₂SO₄(sat.) (MSE) and a slab of glassy carbon were used as reference and counter electrodes, respectively. The reference electrode was separated from the solution by a Luggin–Haber capillary tip. Cyclic voltammetry was used to characterize the catalyst surface area. The Pt active surface area was estimated by three different ways, namely, the charge of hydrogen adsorption/desorption region ($S_{Pt,H}$), the charge of platinum oxide desorption ($S_{Pt,oxide}$), and the charge associated with CO oxidation ($S_{Pt,CO}$). The active surface area of gold was determined from the integration of the oxide reduction regions.

Results and discussion

Physical characterization of the catalysts

Particles' morphology. Fig. 1 shows typical TEM images at low magnifications obtained from the Pt, Au₃₀Pt₇₀, Au₇₀Pt₃₀, Au₈₀Pt₂₀ and Au samples. In all samples, the carbon support was found to be densely populated with the particles. Though the nanoparticles were generally relatively well dispersed on their carbon support, they were sometimes observed to agglomerate heavily. Such examples are illustrated in images (F) and (G) for Au₃₀Pt₇₀ and Au₇₀Pt₃₀, respectively. Their mean size and dispersion were derived according to the relation given by Popa and Balzar¹³ for a log-normal size distribution. Only particles that were non-agglomerated were taken into consideration and the sizes of at least 600 particles were measured for each sample. The nanoparticles were found to become larger with increasing Au content while the ratio of water to surfactant was kept constant at 3.8. The direct measurements of particle size on images are indeed in good agreement with the results obtained using the XRD technique, as indicated in Table 1.

Note that stacking fault probabilities (α) and internal mean strains (σ) are very important for bimetallic materials compared to those obtained for the pure metals.

Fig. 2 shows several representative HRTEM images for samples of Pt (A and B), Au₃₀Pt₇₀ (C), Au₇₀Pt₃₀ (D) and Au (E). On these images, the nanoparticles are viewed along their (011) zone axis. In the bimetallic and pure gold particles, twins have been often observed. Fig. 2C and D show each a twinned nanoparticle of Au₃₀Pt₇₀ and Au₇₀Pt₃₀, respectively. Their twin planes (T) are along the super-imposed dashed lines. Stacking faults (SF) were also observed and one of them is illustrated in Fig. 2E for a Au particle. Twins were never noticed in samples of pure platinum particles. Though the fraction of twinned particles could not be quantified using HRTEM, our observations seem to correlate well with the results derived from X-ray measurements (mean stacking fault probability reported in Table 1, see discussion below). All particles were found to facet preferentially on the crystallographic planes {111} and {100}, and are indicated on Fig. 2. The two types of facets were found to have similar lengths or surface exposed. Along these facets, atomic steps can be visible (Fig. 2A and D). The nanoparticles containing

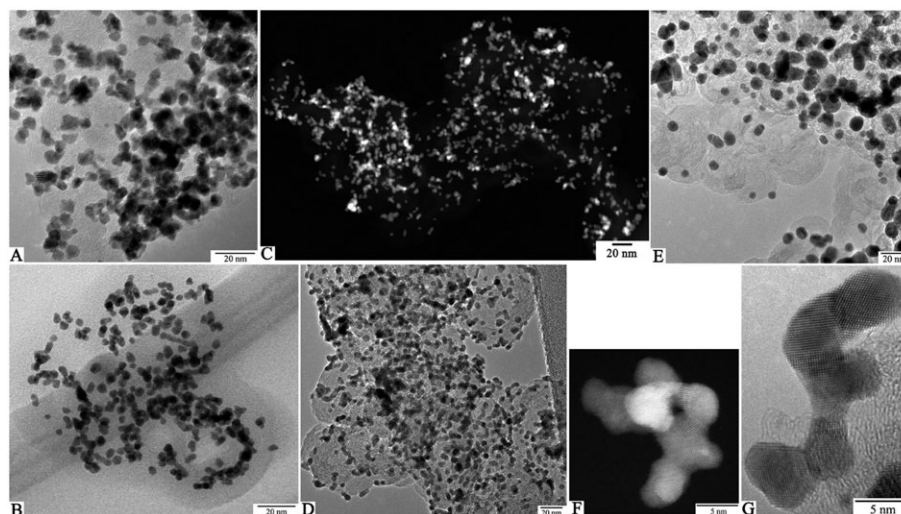


Fig. 1 TEM images of the nanoparticles resting onto their Vulcan carbon support. (A) Pt. (B) Au₃₀Pt₇₀. (C) Au₇₀Pt₃₀. (D) Au₈₀Pt₂₀. (E) Au. Particle agglomerates are shown in (F) and (G) for Au₃₀Pt₇₀ and Au₇₀Pt₃₀, respectively.

Table 1 Structural parameters of Au–Pt catalysts

Au (at%)	$d_{\text{WAXS}}/\text{nm}$	d_{TEM}/nm	α (%)	$\sigma/\text{N mm}^{-2}$	$a/\text{\AA}$
0	3.5	4.1 ± 0.4	1.8	170	3.903
30	4.0	4.1 ± 0.8	5.4	460	3.977
70	4.3	4.3 ± 1.0	7.4	490	4.022
80	5.0	4.5 ± 0.9	8.2	510	4.028
100	9.4	7.5 ± 3.0	5.1	160	4.064

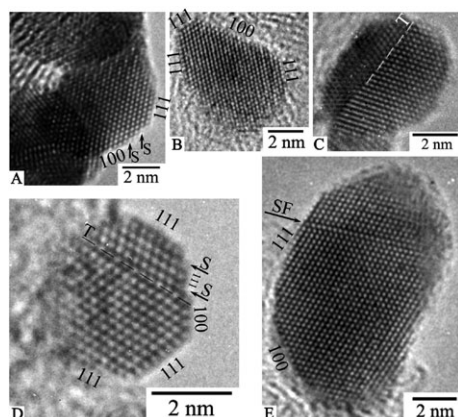


Fig. 2 Several representative HRTEM images. (A and B) Pt. (C) Au₃₀Pt₇₀. (D) Au₇₀Pt₃₀. (E) Au. Note that the globular amorphous carbon support is visible in some of the images. Facets, steps (S), twins (T) and stacking faults (SF) are highlighted.

no twin (Fig. 2A–E) present the classical shape of a truncated octahedron. The presence of twins in nanoparticles generally results in decahedral or icosahedral nanocrystals.^{14,15} These multiply-twinned-particles structures are obtained by assembling tetrahedral units, each in twin relation with its neighbours. In such structure, elastic strain of the fcc structure is necessary in order to fill the space with tetrahedral units.^{16,17} Then, in bimetallic particles, the stress determined from the WAXS measurements (Table 1) can mainly result from the strain inside the multiply-twinned-particles.

X-Ray diffraction analysis. WAXS measurements were performed to characterize the microstructure of Pt, Au₃₀Pt₇₀, Au₇₀Pt₃₀, Au₈₀Pt₂₀ and Au catalysts. Fig. 3 shows the corrected patterns and the fitted profiles obtained with Au and Au₃₀Pt₇₀ catalysts.

The fit with five Pearson VII functions gives two important parameters: the accurate peak positions b and the integral line width, db , in reciprocal b -space, see Fig. 4. There are large variations of the integral line width that are not expected for a simple size broadening. Metal nanoparticles can have large internal stress, varying with the lattice direction represented by the hkl -indices according to the elastic anisotropy. Moreover, they are frequently faulted by departing from the regular

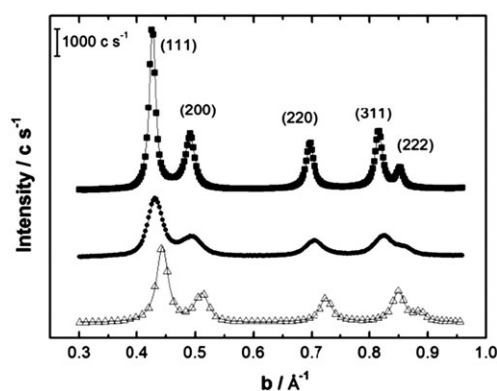


Fig. 3 Diffraction patterns of Pt, Au₇₀Pt₃₀, and Au samples (from bottom). Experimental points (symbols) and fitted profiles (continuous line). The curves are shifted upwards.

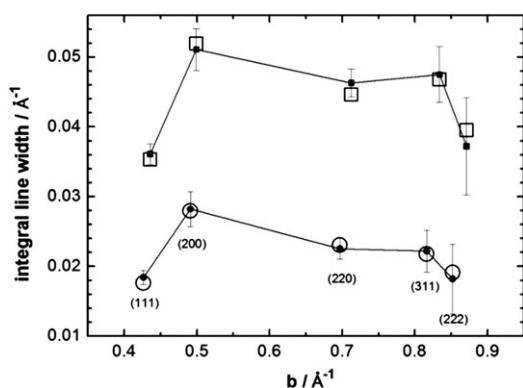


Fig. 4 Williamson-Hall plots obtained with Au and Au₃₀Pt₇₀ samples. Experimental (black symbols) and fitted (open symbols).

stacking periodicity ABCABC, described by a stacking fault probability. In previous papers^{18–20} we have shown that such line width fluctuations can be ascribed to these defects: as a result of the best fit (open symbols in Fig. 4) we obtained the three parameters: mean crystallite size (d), mean stress (σ) and mean stacking fault probability (α). The calculations are confirmed by HRTEM observations.

It is important to notice that twinning is clearly more significant in the alloyed particles than in pure metals.

Taking a closer look into the internal mean stress (σ) and lattice parameter (a) values and comparing the HRTEM observations we arrive at the conclusion that for platinum the stress is an isostatic one since the value of the lattice parameter (a) is relatively small as compared to the one of bulk platinum.

The lattice contraction effect exhibited by platinum nanoparticles is attributed to quantum size effect.^{19,21–23} In fact for particles with a mean diameter of 3.5 nm surface tensions compress the platinum clusters. This effect has been already described by Wasserman *et al.*²⁴ This effect is stronger as the surface to volume ratio increases. Moreover, no twins and no stacking faults are observed for platinum, which confirms the low stacking fault probability (α) value. For Au₇₀Pt₃₀ and Au₈₀Pt₂₀ the value of the lattice parameter (a) is in good agreement with Vegard's law (Fig. 5). Moreover, note that stacking fault probabilities and internal mean strains are very

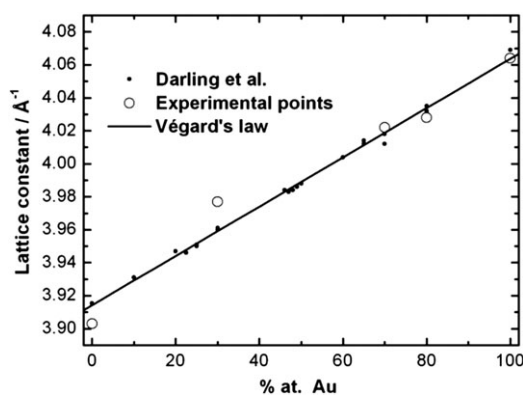


Fig. 5 Experimental lattice parameters of the Au-Pt nanoparticles compared with literature data for bulk Pt-Au alloys obtained by Darling *et al.*²⁵ (small circles).

important for bimetallic materials compared to those obtained for the pure metals. The size of nanoalloyed-particles seems to be higher than for pure platinum which confirms that quantum size effect is negligible. Moreover, no contraction of lattice is observed for bimetallic particles. This can be explained by a weak quantum size effect and an uncertainty of the stoichiometry of alloyed particles.

Moreover the high values of the internal mean stress (σ) and of the stacking fault probability (α) are in good agreement with HRTEM observations, which shows stacking faults and twins in the alloyed particles, *cf.* Fig. 2. This allows to imagine that mean stress represents mainly shear stress.

Nanoalloy analysis. The chemical composition of the different samples has been analysed by XEDS and is in very good agreement with the targeted formulas. As during the spectra acquisition, many particles were illuminated by a large electron beam, in order to have well defined XEDS peaks, these analyses give the global composition of the samples. Using the STEM mode of the probe corrected FEI-Titan, due to the high brightness of the electron probe, it is possible to analyse an individual particle. Fig. 6A and B show the XEDS spectra acquired on individual particle of Au₇₀Pt₃₀ and Au₃₀Pt₇₀, respectively. Note that the Cu peak is an artefact (²⁹Cu K β_1 \approx 8.904 keV) and originates from the fine copper mesh grid supporting the Lacey carbon. The peaks for ⁷⁸Pt ($L\alpha_1 \approx$ 9.441 keV) and ⁷⁹Au ($L\alpha_1 \approx$ 9.711 keV) are indicated on the Figure. Although the number of counts in the peaks is relatively low due to the small analysed volume, quantification was attempted and gives a composition of 69 at% Au for the first sample and of 29 at% for the second one. Their modelled spectra are shown in Fig. 6C. Both elements were quantified for many (around 15) particles and were found to vary only within several atom fractions.

In order to confirm the tendency for Au₃₀Pt₇₀ to form a core/shell structure, as seems to indicate the XRD lattice parameter measurement, a single isolated nanoparticle was probed in its centre (D) and over its entire volume (E). The results are shown in Fig. 6D–F. Once again, although the number of counts in the peaks is small, quantification was attempted. The particle was found to be richer in Au in its core: 43 at% as opposed to 28 at% for the entire particle. Although this quantification cannot be precise, these XEDS analyses are in agreement with a core-shell particle structure.

The close proximity of both elements (⁷⁸Pt and ⁷⁹Au) combined with their near-identical crystalline structure (face centred cubic with a lattice parameter equal to 0.408 nm and 0.392 nm for Au and Pt, respectively) makes it difficult, if not impossible, to image changes either in the z -contrast or bright field TEM images in case a core-shell structure is formed. The only nanoscopic solution to prove the existence of a richer core was through the use of XEDS.

The calculated lattice parameters related to the peak positions are implemented in Fig. 5 which displays the lattice parameter (a) versus Au concentration for the bulk Pt-Au system.²⁵ There is an important deviation from the nominal 30% Au concentration to an apparently higher Au content of 45 at%, whereas the a -parameter of Au₇₀Pt₃₀ and Au₈₀Pt₂₀-samples fits the bulk data. Such apparently higher

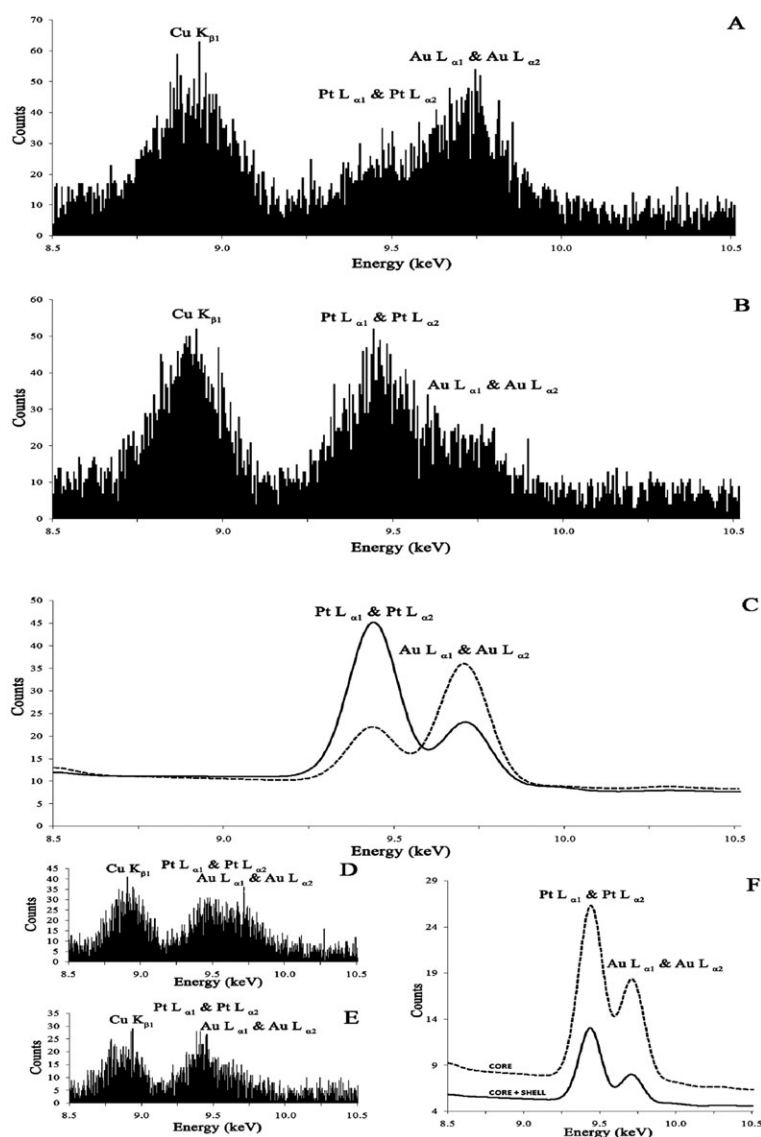


Fig. 6 Montage of four XEDS spectra recorded on two single, distinct and representative nanoparticles and their respective fits. (A) Au₇₀Pt₃₀. (B) Au₃₀Pt₇₀. (C) Model spectra of A and B. (D) Spectrum obtained from the core of a Au₃₀Pt₇₀ particle. (E) Spectrum obtained from the entire same particle. (F) Model spectra of D and E. Note that the ²⁹Cu Kβ₁ ≈ 8.904 keV peak is an artefact and that it originates from the supporting copper grid.

Au content can be alternatively explained by an enrichment of Au atoms in the core, and segregation of the smaller Pt atoms to the particle surface. This result has been already confirmed by Chen *et al.*²⁶ Model calculations for another bimetallic Pt–Ru system have shown that segregation effects do, in fact, modify the net lattice spacing observed in an XRD diagram.²⁷

Surface electrochemistry

Surface probed by oxide layer reduction. The surface of different Au–Pt catalysts has been quantified in terms of active surface for platinum and in terms of chemical composition. Chemical compositions of the surface have been determined by using cyclic voltammetry in an alkaline medium (0.1 M NaOH). The charge associated to the desorption of oxide species can be used to determine the surface composition.^{28,29}

The peak at 1.04 V *vs.* RHE during the negative going scan is associated to the reduction of gold oxide species and the peak at 0.60 V *vs.* RHE is associated to the reduction of platinum oxide species, Fig. 7. For pure materials the charge associated to the reduction of oxide species are 543 μC cm^{−2} and 493 μC cm^{−2} for Pt and Au, respectively.

The atomic content of gold can be deduced as follows:

$$x = \frac{S_{\text{Au}}}{S_{\text{Au}} + S_{\text{Pt}}} \times 100 \quad (3)$$

where x represents the Au content, and S_{Au} and S_{Pt} are the electrode surface covered by gold and platinum oxides, respectively. The results obtained for different Au–Pt catalysts are shown in Table 2.

The values obtained in terms of surface composition for Au₂₀Pt₈₀ suggest a strong segregation effect of platinum at the

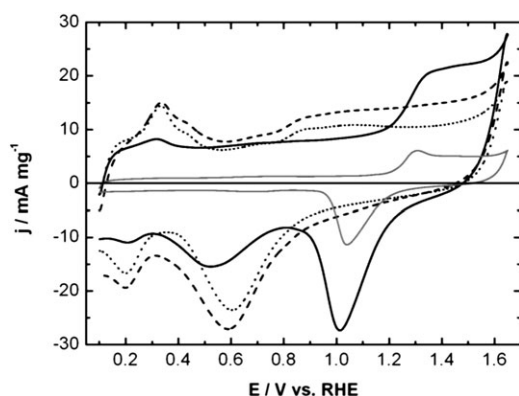


Fig. 7 Voltammograms (after 19 cycles) of Pt (dotted line), Au₂₀Pt₈₀ (dashed line), Au₈₀Pt₂₀ (solid line), and Au (gray line) nanoparticles recorded at 25 °C in alkaline medium (0.1 M NaOH). Scan rate = 20 mV s⁻¹.

surface for catalysts with low gold contents. This observation is in good agreement with the anomalous large lattice parameter calculated from WAXS data for Au₃₀Pt₇₀ catalyst (Fig. 5). Moreover, numerous XEDS measurements were recorded on single isolated particles and were found to consist exclusively of gold and platinum. The XEDS results collected by TEM on isolated particles are in good accordance with the ones collected over larger volumes of the materials in SEM. The global composition of the sample is therefore the same as individual particles, which confirms their alloyed character.

Moreover, the more the gold content increases, the more the surface composition is near the nominal composition of bimetallic compounds. These observations could be in favour of formation of a core-shell structure with Au core and Pt shell for low gold containing catalysts. For higher gold contents it is possible that Au-Pt catalysts surfaces are composed of platinum clusters in the vicinity of gold clusters. The slight shift towards negative potential for the desorption peak of platinum oxides could be the result of the formation of more complex platinum oxides during the positive-going scan.

Surface probed by carbon monoxide oxidation and hydrogen adsorption. The determination of the platinum active surface area was also probed by a CO stripping process. The charge considered was 420 $\mu\text{C cm}^{-2}$, assuming a linear adsorption of the CO molecule on all platinum active sites. This process is believed to be non-electroactive on bulk gold.³⁰ To calculate the platinum active surface area a charge of 210 $\mu\text{C cm}^{-2}$ associated with the hydrogen adsorption/desorption region was taken. The slightly greater estimated

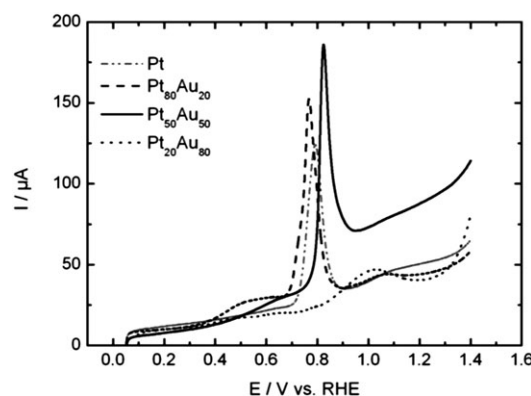


Fig. 8 First forward-scan of CO oxidation voltammograms collected from various Au-Pt catalysts in 0.1 M H₂SO₄ at 5 mV s⁻¹ and at 25 °C.

surface value for Pt, Au₂₀Pt₈₀ and Au₇₀Pt₃₀ using the coulometry of the oxide desorption peak can be explained by an oxidation of more than one monolayer. Moreover, the lower values obtained by coulometry of the CO oxidation peak for Pt and Au₂₀Pt₈₀ can be explained by the non total coverage of the platinum surface by CO. The electrochemical response for different Au-Pt catalysts are shown in Fig. 8.

This Figure clearly shows a shift towards negative potentials for CO oxidation peak on Au₂₀Pt₈₀ catalyst compared to the one obtained for Pt. In fact the CO oxidation peak is centred at 0.79 V vs. RHE for platinum catalyst against 0.76 V vs. RHE for Au₈₀Pt₂₀ catalyst. Moreover, when the gold content increases in the catalyst composition there is a shift towards positive potentials. The oxidation peaks observed on Au₅₀Pt₅₀ and Au₈₀Pt₂₀ catalysts are centred at 0.82 and 1.02 V vs. RHE, respectively. Obviously, the CO oxidation peak becomes broader when the gold content increases. Such observations are in agreement with those already made earlier³¹ by considering CO oxidation on platinum deposited on nanoporous gold blades surfaces. It has been shown that short time deposition leads to a shift of the CO oxidation peak towards positive potentials. This peak broadening can be explained by the isolation of platinum clusters at the particles' surface, considered to be the origin of a more difficult adsorption of hydroxyl species. The movement of the peak towards positive potentials, when gold content increases in the bimetallic composition, can be explained by the alloying effect between gold and platinum, which involves a significant increase in the bonding energy between CO and platinum.³² Note, however, that the active surface area for platinum determined *via* different methods is in good agreement, *cf.* Table 2. This is a

Table 2 Surface composition and active surface area of platinum for different Au-Pt catalysts

	Pt	Au ₂₀ Pt ₈₀	Au ₇₀ Pt ₃₀	Au ₈₀ Pt ₂₀	Au
at% Au	0	0	56	71	100
at% Pt	100	100	44	29	0
$S_{\text{Pt,oxide}}/\text{cm}^2$	5.6	6.4	2.6	2.0	
$S_{\text{Pt,H}}/\text{cm}^2$	5.3	5.5	2.0	2.3	
$S_{\text{Pt,CO}}/\text{cm}^2$	4.5	4.6	2.3	2.3	

strong indication that gold nanocatalysts are indeed inactive towards CO oxidation.

Taking a closer look into Fig. 8, one observes a pre-wave centred at 0.5 V vs. RHE on Au₂₀Pt₈₀ at ca. 0.6 V vs. RHE on Au₅₀Pt₅₀ and Au₈₀Pt₂₀. This pre-wave could be attributed to the oxidation of CO molecules in the vicinity of surface defects where the formation of water discharge species occurs at lower potentials.³³ In the case of platinum catalysts the intensity of this pre-wave is very weak as compared to the intensity of the CO oxidation peak located at 0.79 V vs. RHE. This ratio of intensity is much more important in the case of other Au_xPt_y catalysts. Therefore, it seems to be possible to attribute these different ratios to different amounts of surface defects in Au_xPt_y catalysts. Moreover the CO oxidation in the pre-wave potential region could lead to a significant increase in the bonding energy between CO and platinum because of the weaker interaction between adsorbed CO molecules resulting from the formation of CO islands.³³ These phenomena could be at the origin of a shift of the CO oxidation peak towards positive potentials. This interpretation could explain why there is an increasing peak broadening with the rising gold content in the catalyst composition. This broadening could be the result of two different effects: the ligand effect in the alloys and the presence of surface defects.

Conclusions

Nanoscale Au–Pt alloy catalysts were synthesized by w/o microemulsion to use them as catalysts for CO oxidation. Physicochemical characterizations (WAXS) of the bimetallic nanoparticles were correlated with those obtained by electrochemical measurements for Au–Pt catalyst. A segregation effect of platinum at the surface was shown for low gold content catalysts and high gold content catalysts exhibited alloy properties. The obtained Au–Pt catalysts are responsible for a shift of the CO oxidation peak. Platinum active surface measurements realized by three different methods seem to indicate that gold in these nanoparticles is inactive towards CO-oxidation. This kind of catalyst activates the anodic reaction (glucose oxidation) of a biofuel cell.^{20,34,35} A deeper insight will be however led by the use of *in situ* spectroscopic studies.

Acknowledgement

W. V. is grateful for the financial support from the National Science Council (under contract number NSC96-2113-M-008-008) and the National Central University, Taiwan, ROC.

The authors acknowledge “le Conseil Regional de Poitou-Charentes” for financial support.

References

- 1 F. H. B. Lima, J. Zhang, M. H. Shao, K. Sasaki, M. B. Vukmirovic, E. A. Ticianelli and R. R. Adzic, *J. Phys. Chem. C*, 2007, **111**, 404–410.
- 2 E. Bus and J. A. van Bokhoven, *J. Phys. Chem. C*, 2007, **111**, 9761–9768.
- 3 B. Hvolbæk, T. V. W. Janssens, B. S. Clausen, H. Falsig, C. H. Christensen and J. K. Nørskov, *Nanotoday*, 2007, **2**, 14–18.
- 4 R. W. Reeve, P. A. Christensen, A. J. Dickinson, A. Hamnett and K. Scott, *Electrochim. Acta*, 2000, **45**, 4237–4250.
- 5 R. W. Reeve, P. A. Christensen, A. Hamnett, S. A. Haydock and S. C. Roy, *J. Electrochem. Soc.*, 1998, **145**, 3463–3471.
- 6 H. Tributsch, M. Bron, M. Hilgendorff, H. Schulenburg, I. Dorbandt, V. Eyert, P. Bogdanoff and S. Fiechter, *J. Appl. Electrochem.*, 2001, **31**, 739–748.
- 7 M. L. Wu, D. H. Chen and T. C. Huang, *Chem. Mater.*, 2001, **13**, 599–606.
- 8 I. Capek, *Adv. Colloid Interface Sci.*, 2004, **110**, 49–74.
- 9 L. G. R. A. Santos, C. H. F. Oliveira, I. R. Moraes and E. A. Ticianelli, *J. Electroanal. Chem.*, 2006, **596**, 141–148.
- 10 W. Vogel, B. Tesche and W. Schulze, *Chem. Phys.*, 1983, **74**, 137–142.
- 11 B. E. Warren, *X-Ray Diffraction*, Addison Wesley, Reading, MA, 1969.
- 12 W. Vogel, *Appl. Phys. A*, 1996, **62**, 295–301.
- 13 N. C. Popa and D. Balzar, *J. Appl. Cryst.*, 2002, **35**, 338–346.
- 14 S. Ino, *J. Phys. Soc. Jpn.*, 1966, **21**, 346–362.
- 15 P.-A. Buffat, M. Flüeli, R. Spycher, P. Stadelmann and J.-P. Borel, *Faraday Discuss.*, 1991, **92**, 173–187.
- 16 A. Howie and L. D. Marks, *Philos. Mag.*, 1984, **A49**, 95–109.
- 17 L. D. Marks, *Surf. Sci.*, 1985, **150**, 302–318.
- 18 W. Vogel, B. Tesche and W. Schulze, *Chem. Phys.*, 1983, **74**, 137–142.
- 19 W. Vogel, J. Bradley, O. Vollmer and I. Abraham, *J. Phys. Chem. B*, 1998, **102**, 10853–10859.
- 20 A. Habrioux, E. Sibert, K. Servat, W. Vogel, K. B. Kokoh and N. Alonso-Vante, *J. Phys. Chem. B*, 2007, **111**, 10329–10333.
- 21 A. I. Frenkel, C. W. Hills and R. G. Nuzzo, *J. Phys. Chem. B*, 2001, **105**, 12689–12703.
- 22 D. Mott, J. Luo, A. Smith, P. N. Njoki, L. Wang and C.-J. Zhong, *Nano. Res. Lett.*, 2007, **2**, 12–16.
- 23 W. Vogel, *J. Phys. Chem. C*, 2008, **112**, 13475–13482.
- 24 H. J. Wasserman and J. S. Vermaak, *Surf. Sci.*, 1972, **32**, 168–174.
- 25 A. S. Darling, R. A. Mintern and J. C. Chaston, *J. Instrum. Methods*, 1952, **81**, 1952–1953.
- 26 H. M. Chen, H. C. Peng, R. S. Liu, S. F. Hu and L. Y. Jang, *Chem. Phys. Lett.*, 2006, **420**, 484–488.
- 27 W. Vogel, P. Britz, H. Bonnemann, J. Rothe and J. Hormes, *J. Phys. Chem. B*, 1997, **101**, 11029–11036.
- 28 L. D. Burke, J. M. Moran and P. F. Nugent, *J. Solid State Electrochem.*, 2003, **7**, 529–538.
- 29 M. W. Breiter, *Trans. Faraday. Soc.*, 1965, **61**, 749–754.
- 30 P. Diao, D. F. Zhang, M. Guo and Q. Zhang, *J. Catal.*, 2007, **250**, 247–253.
- 31 X. Ge, R. Wang, P. Liu and Y. Ding, *Chem. Mater.*, 2007, **19**, 5827–5829.
- 32 M. Ø. Pedersen, S. Helveg, A. Ruban, I. Stensgaard, E. Lægsgaard, J. K. Nørskov and F. Besenbacher, *Surf. Sci.*, 1999, **426**, 395–409.
- 33 N. P. Lebedeva, M. T. M. Koper, E. Herrero, J. M. Feliu and R. A. V. Santen, *J. Electroanal. Chem.*, 2000, **487**, 37–44.
- 34 A. Habrioux, K. Servat, K. B. Kokoh and N. Alonso-Vante, *Electrochem. Soc. Trans.*, 2007, **7**, 9–18.
- 35 A. Habrioux, K. Servat, S. Tingry and K. B. Kokoh, *Electrochem. Commun.*, 2009, **11**, 111–113.